Pre-print submitted version

Potential and limitations of $CsBi_3I_{10}$ as photovoltaic material

Paz Sebastia-Luna,[a] María C. Gélvez-Rueda,[b] Chris Dreessen,[a] Michele Sessolo,[a] Ferdinand C. Grozema,[b] Francisco Palazon,[a*] and Henk J. Bolink[a]

[a.] Instituto de Ciencia Molecular, ICMol, Universidad de Valencia, St. Catedrático J. Beltrán 2, 46980 Paterna, Spain

[b.] Department of Chemical Engineering, Opto-electronic Materials Section, Delft University of Technology, van der Maasweg 9, 2629 HZ Delft, The NetherlandsAddress here

* Corresponding author: francisco.palazon@uv.es

Abstract

Herein we demonstrate the dry synthesis of $CsBi_3I_{10}$ both as free-standing material as well as in the form of homogeneous thin films, deposited by thermal vacuum deposition. Chemical and optical characterization shows high thermal stability, phase purity, and photoluminescence centered at 700 nm, corresponding to a bandgap of 1.77 eV. These characteristics make $CsBi_3I_{10}$ a promising low-toxicity material for wide bandgap photovoltaics. Nevertheless, the performance of this material as a semiconductor in solar cells remains rather limited, which can be at least partially ascribed to a low charge carrier mobility, as determined from pulsed-radiolysis, time-resolved microwave conductivity. Further developments should focus on understanding and overcoming the current limitations in charge mobility, possibly by compositional tuning through doping and/or alloying, as well as optimizing thin film morphology which may be another limiting factor.

1. Introduction

Lead halide perovskites (LHPs) have attracted a lot of attention over the past decade as a new family of semiconducting materials. Single-junction solar cells made thereof have been demonstrated with power conversion efficiencies (PCEs) of 25.2%, very close to record values for silicon photovoltaics (PV).[1] Furthermore, LHPs possess a number of advantages over silicon and other inorganic semiconductors, such as a high degree of bandgap tunability and low-temperature processing. On the other side, LHPs, as well as other PV materials such as CdTe or GaAs, are composed of highly-toxic elements (Pb, Cd, As), which might undermine their widespread application.[2] Therefore, in parallel with the development of high-efficiency LHP solar cells, the focus is now shifting towards finding and developing low-toxicity, alternative semiconductors. While the fast pace at which these are proposed is exciting, it is also important to assess their potential critically.3 In this context, a few publications have suggested $CsBi_3I_{10}$ as a promising candidate, reporting PCEs from 0.13% to 1.5%.[4–7]

Motivated by these results, we demonstrate hereafter that $CsBi_3I_{10}$ can be synthesized as a free-standing powder (non-templated synthesis) as well as thin films by fully-dry approaches, thus also avoiding the toxicity of most common organic solvents.[8–13] $CsBi_3I_{10}$ powders are synthesized by a simple mechanochemical route (neat ball-milling) whereas thin films are prepared by dual-source thermal vacuum co-deposition of CsI and BiI_3. Physical and chemical characterizations reveal that the as-prepared materials show crystallinity and stoichiometry corresponding to the expected $CsBi_3I_{10}$ phase, with an optical bandgap of approximately 1.77 eV. Semiconductors with such a bandgap are highly sought after for front-cell absorbers in tandem solar cells.[14–16] The thin films are also found to be rather smooth (RMS roughness below 7 nm) with homogeneous photoluminescence as evidenced by hyperspectral imaging.

Despite these encouraging characteristics, the implementation of this material in solar cells results in rather low photovoltaic performance, in line with previous reports (PCE = 0.13%).[6,17] Importantly, we find that with the chosen electron- and hole-transport layers, the direct p-n junction (without $CsBi_3I_{10}$) yields a higher PCE. These low performances may be partially ascribed to film morphology (small grains). Nevertheless, pulsed-radiolysis time-resolved microwave conductivity (PR-TRMC) measurements also reveal that despite an extraordinary long charge carrier lifetime of up to tens of microseconds (pointing to a low defect density), the effective mobility is limited to about 0.024 cm^2/Vs, two orders of magnitude lower than that of LHPs.[18] In

view of this, it is worth reconsidering the potential of this material. Indeed, while the direct bandgap of 1.77 eV (photoluminescence centered at 700 nm) and the possibility of the solvent-free synthesis demonstrated herein are promising, the intrinsic charge carrier mobility should be greatly enhanced (possibly through doping or other compositional tuning) for an efficient use of this material in photovoltaics.

2. Results and Discussion

Mechanochemical synthesis of free-standing CsBi3I10

Non-templated $CsBi_3I_{10}$ powders were synthesized by neat ball-milling of CsI and BiI_3 in 1:3 molar ratio under inert atmosphere (see Experimental Section for details). X-ray diffraction, optical characterization, and thermogravimetric analysis of the as-obtained materials are presented in Figure 1.

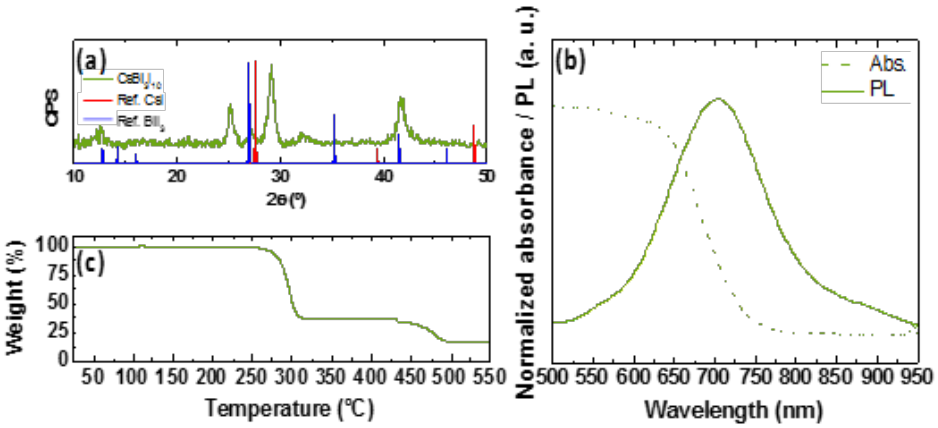

Fig. 1 (a) X-ray diffractogram of the $CsBi_3I_{10}$ powders (green line) and reference patterns for CsI (red; ICSD 44938) and BiI_3 (blue; ICSD 56573) (b) normalized absorbance and photoluminescence spectra (excitation wavelength 522 nm) and (c) thermogravimetric analysis (TGA) of $CsBi_3I_{10}$ powders.

The X-ray diffractogram (XRD) of the powder after ball-milling is shown in Figure 1a. The first observation that can be made is that several major peaks of the binary precursors are absent. Since the powder sample is not expected to have any major preferential orientation which could otherwise explain the suppression of selected peaks, it is reasonable to conclude that CsI and BiI_3 have fully reacted. While we did not find a reference pattern for $CsBi_3I_{10}$ in the Inorganic Crystal Structure Database (ICSD) or other databases, we note that the diffractogram obtained

here matches the expected peaks and relative intensities for $CsBi_3I_{10}$, based on previously published data.[6] In this article, Johansson et al. suggest that $CsBi_3I_{10}$ crystallizes in a structure that is closely related to that of BiI_3 and $Cs_3Bi_2I_9$, which is another stable ternary phase. This explains some similarities in the XRD patterns between the three phases. Such similarities have also been observed by others.[4,5] Nevertheless, if we compare our diffractogram to the reference pattern of $Cs_3Bi_2I_9$ (Figure S1) it becomes apparent that several major peaks of the latter are not present, pointing to the absence of $Cs_3Bi_2I_9$. We can thus conclude that $Cs_3Bi_2I_{10}$ is formed, with the full reaction of binary precursors and without the formation of other ternary phases.

This conclusion is further supported by optical characterization. The optical absorption and photoluminescence (PL) spectra are presented in Figure 1b. We observe an absorption onset and PL peak centered around 700 nm, corresponding to an optical bandgap of 1.77 eV (see Tauc plot in Figure S2). This is in good agreement with previously-reported values[17,19] and different from the emission of $Cs_3Bi_2I_9$ which is centered at 650 nm.[20] Importantly, the difference between the cut-off of the absorption spectrum and the PL maximum (Stokes-shift) is small. This feature, together with the steep absorption onset, is expected for direct bandgap semiconductors, where the charge carrier generation and recombination occur at the band edges. The direct bandgap of 1.77 eV for as-prepared $Cs_3Bi_2I_{10}$ is of particular interest in wide bandgap solar cells for tandem applications.[21]

In order to assess the thermal stability of this material, we have also conducted thermogravimetric analyses (TGA; Figure 1c). The curve shows a first weight loss of 68% around 275 °C, followed by a second loss from the remaining 32% to 13% of the initial mass, around 475 °C. These losses can be rationalized by considering the following degradation mechanism:

(1) $3\ Cs_3Bi_2I_{10}\ (s) = Cs_3Bi_2I_9\ (s) + 7\ BiI_3\ (g)$, around 275 °C

(2) $Cs_3Bi_2I_9\ (s) = 3\ CsI\ (s) + 2\ BiI_3\ (g)$, around 475°C

Considering the molecular weights and stoichiometry involved in each of the two steps, the observed weight losses are fully consistent with the expected values. The thermal stability of $CsBi_3I_{10}$ up to around 250 °C is significantly higher than that of the most common hybrid organic-inorganic lead halide perovskites.[22,23] Moreover, it is well beyond the usual range of operation of most optoelectronic devices, which ensures that no thermal-induced degradation should occur.

Vacuum-deposited thin films

In order to fabricate PV devices, we tested the deposition of $CsBi_3I_{10}$ as a thin film. Reported procedures so far are based on the dissolution of the inorganic salts in an organic solvent and subsequent spin-coating.24 Nevertheless, typical solvents such as DMF used for this approach are highly toxic and generate a considerable amount of waste. Hence, using them partly defeats the purpose of developing this low-toxicity material. Therefore, we used thermal vacuum deposition instead. Ideally, as-synthesized $CsBi_3I_{10}$ powders could be used to fabricate thin films by single-source vacuum deposition (SSVD).[25,26] Nevertheless, our attempts at depositing $CsBi_3I_{10}$ films by SSVD resulted in the decomposition of $CsBi_3I_{10}$ into $Cs_3Bi_2I_9$ + BiI_3, with the latter subliming at much lower temperature and with a higher deposition rate than the former. Consequently, thin films were fundamentally composed of BiI_3, while $Cs_3Bi_2I_9$ was found to remain in the crucible (see Figures S3-S4). These observations are consistent with the first degradation mechanism observed by TGA (see discussion above) and highlight the fact that it cannot be avoided here despite fast heating in vacuum.

Therefore, we used an alternative method to prepare thin films by co-deposition of CsI and BiI_3 from two thermal sources in a vacuum chamber (base pressure 10^{-6} mbar), each set at a suitable temperature to adjust the deposition rates (see Experimental Section for details).

In situ, temperature-dependent XRD (Figure 2a) shows the evolution of the $CsBi_3I_{10}$ thin-film structure from room temperature (RT) to 150 °C, which is different from the diffractogram of the same compound in the powder state (Figure 1a). Nevertheless, a comparison with published data from Johansson et al.[6] shows that the main peaks observed here around $2\theta = 12.7°$ and $2\theta = 25.6°$ may be indexed as the (003) and (006) planes of the crystal structure suggested therein. This reveals that the thin film has a preferential orientation with the [001] direction being perpendicular to the substrate. Such a texture (preferential orientation) is common in thin films and explains the differences observed between the XRD signals of powders (Figure 1a) and thin films (Figure 2a) of the same material.[27] Interestingly, the diffractogram remains mostly unchanged from room temperature to 150 °C, denoting that no phase transformation occurs in this range. Peak shifts are also minimal (around 0.1° - 0.2°), pointing to a very limited thermal expansion of this material. It must be noted, though, that other chemical variations such as the presence (before or after annealing) of metallic bismuth, as observed by others,[4] could not be discarded. In order to determine the ratio of the different elements present in the thin film, X-ray photoelectron spectroscopy (XPS) was performed. Films were previously annealed at different temperatures to check if this process can help the formation of the desired stoichiometry. The

different ratios of Cs, Bi and I calculated for each temperature tested (pristine, 50 °C and 80 °C) are reported in Table S1. The ratios might suggest that an increase in the annealing temperature of the films favors the formation of a stoichiometry closer to the nominal one, as the Cs:Bi:I ratio obtained at 80 °C (Figure 2b) is 1.0 : 3.4 : 10. However, it must be noted that XPS is a surface-sensitive technique (depth of analysis around 2 nm – 10 nm). Hence, the different values obtained in this temperature range are most likely due to the diffusion of different species to the surface. Optical absorption and photoluminescence (Figure 2c) spectra show the expected features for CsBi3I10, which are significantly different from those of $Cs_3Bi_2I_9$, as previously discussed. A close look at absorption and emission properties of the thin film and powder sample show slight differences (see Figures S2 and S5). Indeed, the absorption onset (or onset of Tauc plot) is blue-shifted by about 70 meV (Figure S2) in the film. Similar thickness-dependent blue-shifts have previously been observed on thin films in this range of thicknesses.[28,29] This behavior has been ascribed to the small grain size present in thinner films. On the contrary, the powder is expected to be highly polydisperse in crystal size. This is coherent with a red-shifted absorption dominated by the larger crystallites and a slightly wider photoluminescence peak (see Figure S5).

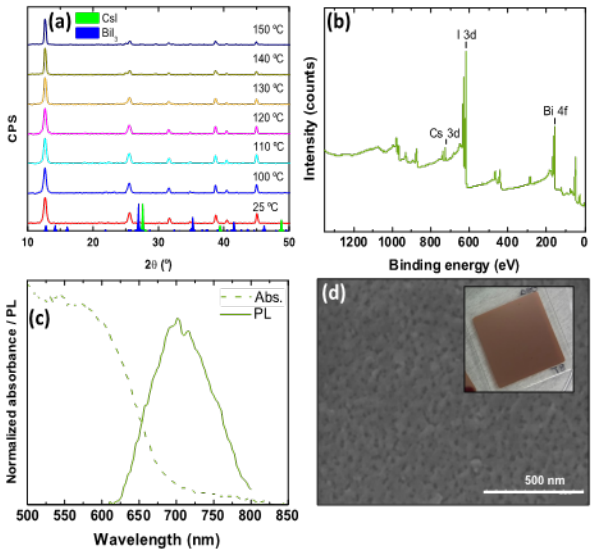

Fig. 2 Characterization of co-evaporated $CsBi_3I_{10}$ thin film (the film is previously annealed at 80 °C for b, c, and d; final thickness of 80 nm). (a) XRD at variable temperature, (b) XPS survey spectrum, (c) normalized absorbance and photoluminescence spectra (excitation wavelength 532 nm), (d) scanning electron microscope (SEM) image and optical photograph (inset).

Concerning the film morphology, from a macroscopic point of view, a smooth surface is observed without any obvious inhomogeneity over a 3 cm x 3 cm substrate (see Figure 2d, inset). Scanning electron microscopy (SEM; Figure 2d) reveals a small-grained surface (typical grain size below 100 nm), again without any obvious inhomogeneity or pinholes at the microscale. Furthermore, the surface roughness was evaluated by atomic force microscopy (AFM; Figure S6) and a root mean squared value (RMS) of 6.95 nm was determined over an area of 2.6 μm^2. The homogeneity of the thin film was further evaluated in terms of optical characteristics through hyperspectral photoluminescence microscopy (Figure 3). The PL spectra for two different regions of the film (marked as blue and red) are presented along with the average PL spectra for the full field of view. The film presents regions with higher and lower PL intensity as directly observed from the brighter and darker spots in Figure 3b and the corresponding different intensities of the PL spectra (Figure 3a). Nevertheless, the differences in intensity are less than one order of magnitude. Furthermore, the PL peak maximum and width are very similar. Again, this points to a high homogeneity in the vacuum-deposited thin film.

In order to gain more insight into the energy levels of this material, air photoemission spectroscopy (APS) was measured (see Figure S7). The ionization energy, which corresponds to the valence band maximum (VBM) for an intrinsic semiconductor such as CsBi3I10, is found to be -6.0 eV, in close agreement with previously reported values for these species (-5.9 eV) and measured with different techniques.[19,30] The energy corresponding to the conduction band maximum (CBM) can be estimated to -4.2 eV by subtracting the bandgap energy to the VBM, as shown in Table S2.

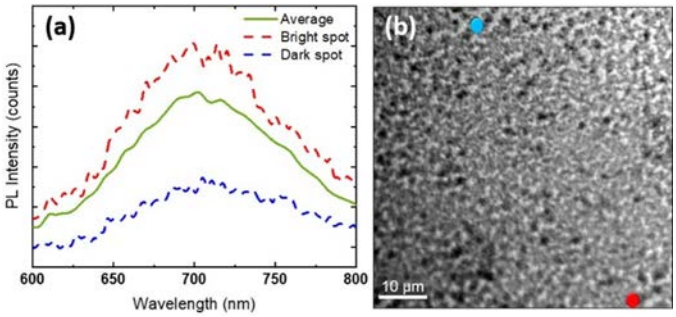

Fig. 3 (a) PL spectra (averaged, bright and dark parts) of the surface of the co-evaporated thin-film, represented in (b). The blue dot corresponds to the dark spot and the red one, to the bright one. NB: Green spectrum in panel (a) is the same as plotted in Figure 2c. Excitation wavelength: 532 nm.

Implementation in solar cells

Given the promising characteristics of co-evaporated $CsBi_3I_{10}$ thin films for photovoltaics, we implemented them in single-junction solar cells. Indium tin oxide (ITO)-coated glass substrates were used as the transparent electrode. A suspension of SnO2 nanoparticles was deposited by spin-coating onto ITO (obtaining a 30 nm thick film) and then covered with a layer of C60 (10 nm) by thermal evaporation. Then, a 210 nm-thick film of $CsBi_3I_{10}$ was deposited by co-evaporation and annealed at different temperatures. Subsequently, N4,N4,N4′,N4′-tetra([1,1′-biphenyl]-4-yl)-[1,1′:4′,1′-terphenyl]-4,4′-diamine (TaTm, 15 nm) and MoO_3 (5 nm) were deposited on top and the device was finished with a gold electrode (100 nm). Current density-voltage (J-V) curves were collected under illumination from a solar simulator (Figure 4a). Independently on the thermal annealing of the $CsBi_3I_{10}$ film, the devices performed poorly with a PCE around 0.12%-0.13%. Surprisingly, the equivalent device without $CsBi_3I_{10}$ (that is with direct contact between C60 and TaTm) outperformed these. These poor performances might be partly ascribed to the small-grained morphology of the $CsBi_3I_{10}$ films as seen by SEM (Figure 2d). Indeed, the moderate gain in short-circuit current after annealing could indicate a beneficial effect from grain sintering. This can be observed by the sharpening of X-ray diffraction peaks, denoting larger crystallites (see Figure S8). Nevertheless, performances remain poor in all annealing conditions. Furthermore, we exclude misalignment of the energy levels of the transport layers with $CsBi_3I_{10}$ as responsible for the large performance losses observed here, as depicted in Figure S9. In order to shed more light into the poor performance of $CsBi_3I_{10}$-based devices, we conducted pulse-radiolysis time-resolved microwave conductivity (TRMC) measurements (see Figure 4b, c). Through these measurements, it was determined that the mobility of charge carriers in the material is around 0.024 cm^2/Vs. This value is about two to three orders of magnitude lower than common values reported for lead halide perovskites, especially measured with the same technique,[18,31–33] and may explain the low short-circuit current obtained in the solar cells. As the exact crystal structure could not be solved, it is not straightforward to give a precise reason for this low charge mobility. Nevertheless, the lifetime of the charge carriers is extraordinarily long (up to tens of microseconds as evidenced in Figure 4c). This long lifetime suggests that the density of defects in the material is low. This is supported by the pulse length dependence (variation of the initial concentration of charge carriers) experiments that show that the recombination dynamics follow second-order recombination (the height of the conductivity signal and lifetime decay is faster as more charge carriers are generated in the material) without indication of trap filling during the pulse. This latter behavior has been previously observed in lead halide perovskites studied with the same experimental technique.[32,33] Therefore, it seems that the low mobility should be addressed rather

by doping or another compositional tuning than by passivating quenching traps, which do not seem to be prevalent.

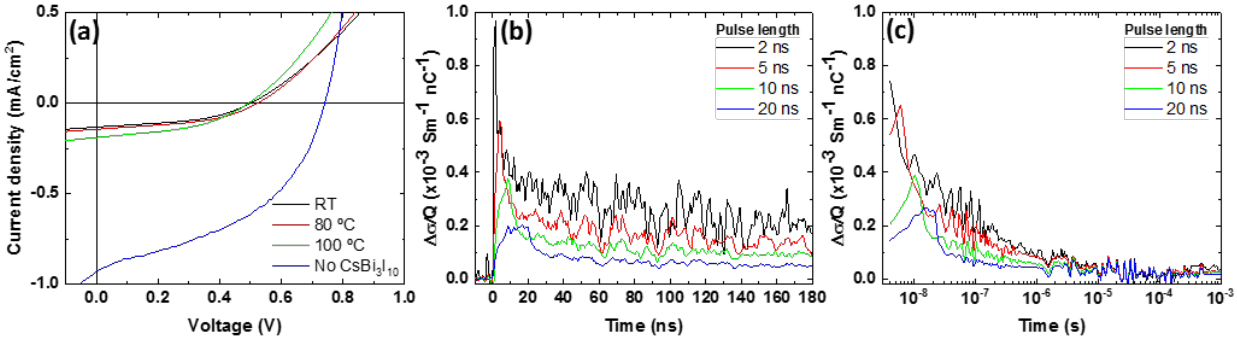

Fig. 4 (a) J–V characteristics under 1 sun illumination of different solar cells made with $CsBi_3I_{10}$ annealed at different temperatures as well as without $CsBi_3I_{10}$. (b and c) Pulse radiolysis TRMC of $CsBi_3I_{10}$ as a function of pulse length (which results in initial concentrations of charge carriers from 1x1016 cm-3 to 2x1017 cm-3). Panel (a) and (b) vary by time scale only.

Conclusions

In summary, we have proposed an alternative, faster and greener method for the synthesis of CsBi3I10, a low-toxicity ternary metal halide with potential use in optoelectronics. This material shows high thermal stability in air and photoluminescence centered at 700 nm, which endorses its application in the fabrication of photovoltaic devices. In addition, we have achieved thin-film deposition of the same material through thermal vacuum co-deposition and implemented it in solar cells. Nevertheless, these devices performed poorly, probably as a result of the low charge carrier mobility demonstrated by pulsed-radiolysis microwave conductivity measurements. Ongoing developments are focused on a precise understanding of the causes of this low mobility and possible solutions, including compositional engineering in multi-cation and multi-anion derivatives as well as doping.

Conflicts of interest

There are no conflicts to declare.

Acknowledgements

The research leading to these results has received funding from the European Union Programme for Research and Innovation Horizon 2020 (2014-2020) under the Marie Skłodowska-Curie Grant Agreement PerovSAMs No. 747599, from the European Research Council (ERC) under the European Union's Horizon 2020 research and innovation programme (Grant agreement No.

[834431]), the Spanish Ministry of Science, Innovation and Universities (ex-MINECO) via the Unidad de Excelencia Marı´a de Maeztu MDM-2015-0538, MAT2017- 88821-R, and PCIN-2015-255, and the Generalitat Valenciana (Prometeo/2016/135). P.S thanks the Spanish Ministry of Education, Culture and Sport for her pre-doctoral grant. C. D. states that the project that gave rise to these results received the support of a fellowship from “la Caixa” Foundation (ID 100010434). The fellowship code is LCF/BQ/DI19/11730020. M.S. thanks the Spanish Ministry of Science Innovation and Universities (ex-MINECO) for his postdoctoral RyC contract. We acknowledge the European Union’s Horizon 2020 research & innovation program under grant agreement No. 763977 of the PerTPV project. We also thank María Dolores Jordán for performing the XPS measurements and Alejandra Soriano for the AFM characterization.

Notes and references

1 NREL, Best Research-Cell Efficiency Chart., https://www.nrel.gov/pv/cell-efficiency.html, (accessed 7 August 2019).

2 W. Ke and M. G. Kanatzidis, Nat. Commun., 2019, 1–4.

3 J. Euvrard, X. Wang, T. Li, Y. Yan and D. B. Mitzi, J. Mater. Chem. A, 2020, 8, 4049–4054.

4 D. B. Khadka, Y. Shirai, M. Yanagida and K. Miyano, J. Mater. Chem. C, 2019, 7, 8335–8343.

5 X. W. Tong, W. Y. Kong, Y. Y. Wang, J. M. Zhu, L. B. Luo and Z. H. Wang, ACS Appl. Mater. Interfaces, 2017, 9, 18977–18985.

6 M. B. Johansson, H. Zhu and E. M. J. Johansson, J. Phys. Chem. Lett., 2016, 7, 3467–3471.

7 L. Luo, X. Tong, Z. Zhang, D. Wang, C. Xie and Y. Wu, J. Mater. Chem. C, 2019, 7, 863–870.

8 B. A. Rosales, L. Wei and J. Vela, J. Solid State Chem., 2018, 271, 206–215.

9 Z. Hong, D. Tan, R. A. John, Y. K. E. Tay, Y. K. T. Ho, X. Zhao, T. C. Sum, N. Mathews, F. García and H. Sen Soo, iScience, 2019, 312–325.

10 D. Prochowicz, M. Saski, P. Yadav, M. Grätzel and J. Lewiński, Acc. Chem. Res., 2019, 52, 3233–3243.

11 F. Palazon, Y. El Ajjouri and H. J. Bolink, Adv. Energy Mater., 2019, 1902499, 1–13.

12 J. Ávila, C. Momblona, P. P. Boix, M. Sessolo and H. J. Bolink, Joule, 2017, 1, 431–442.

13 D. Prochowicz, M. Franckevičius, A. M. Cieślak, S. M. Zakeeruddin, M. Grätzel, J. Lewiński, F. Franckevičius, A. M. Cié, S. M. Zakeeruddin, M. Grätzelgrätzel and J. Lewí, J. Mater. Chem. A, 2015, 3, 20772–20777.

14 A. Manekkathodi, B. Chen, J. Kim, S. W. Baek, B. Scheffel, Y. Hou, O. Ouellette, M. I. Saidaminov, O. Voznyy, V. E. Madhavan, A. Belaidi, S. Ashhab and E. Sargent, J. Mater. Chem. A, 2019, 7, 26020–26028.

15 M. I. Hossain, W. Qarony, V. Jovanov, Y. H. Tsang and D. Knipp, J. Mater. Chem. A, 2018, 6, 3625–3633.

16 T. Leijtens, K. A. Bush, R. Prasanna and M. D. McGehee, Nat. Energy, 2018, 3, 828–838.

17 H. Zhu, M. B. Johansson and E. M. J. J. Johansson, ChemSusChem, 2018, 11, 1114–1120.

18 L. M. Herz, ACS Energy Lett., 2017, 2, 1539–1548.

19 J. Shin, M. Kim, S. Jung, C. S. Kim, J. Park, A. Song, K. B. Chung, S. H. Jin, J. H. Lee and M. Song, Nano Res., 2018, 11, 6283–6293.

20 Y. El Ajjouri, V. S. Chirvony, N. Vassilyeva, M. Sessolo, F. Palazon and H. J. Bolink, J. Mater. Chem. C, 2019, 7, 6236–6240.

21 Q. Wali, N. K. Elumalai, Y. Iqbal, A. Uddin and R. Jose, Renew. Sustain. Energy Rev., 2018, 84, 89–110.

22 G. Niu, W. Li, J. Li, X. Liang and L. Wang, RSC Adv., 2017, 7, 17473–17479.

23 T. T. Ava, A. Al Mamun, S. Marsillac and G. Namkoong, Appl. Sci., 2019, 9, 188.

24 G.-X. Liang, X.-Y. Chen, Z.-H. Chen, H.-B. Lan, Z.-H. Zheng, P. Fan, X.-Q. Tian, J.-Y. Duan, Y.-D. Wei and Z.-H. Su, J. Phys. Chem. C, 2019, 123, 27423–27428.

25 Y. El Ajjouri, F. Palazon, M. Sessolo and H. J. Bolink, Chem. Mater., 2018, 30, 7423–7427.

26 M. J. Crane, D. M. Kroupa, J. Y. Roh, R. T. Anderson, M. D. Smith and D. R. Gamelin, ACS Appl. Energy Mater., 2019, 2, 4560–4565.

27 P. Sebastia-Luna, J. Navarro-Alapont, M. Sessolo, F. Palazon and H. J. Bolink, Chem. Mater., 2019, 31, 10205–10210.

28 S. A. Aly and A. A. Akl, Chalcogenide Lett., 2015, 12, 489–496.

29 M. Ben Rabeh, N. Khedmi, M. A. Fodha and M. Kanzari, Energy Procedia, 2014, 44, 52–60.

30 Z. Liu, S. Dai, Y. Wang, B. Yang, D. Hao, D. Liu, Y. Zhao, L. Fang, Q. Ou, S. Jin, J. Zhao and J. Huang, Adv. Funct. Mater., 2020, 30, 1906335.

31 N. T. P. Hartono, S. Sun, M. C. Gélvez-Rueda, P. J. Pierone, M. P. Erodici, J. Yoo, F. Wei, M. Bawendi, F. C. Grozema, M. J. Sher, T. Buonassisi and J. P. Correa-Baena, J. Mater. Chem. A, 2019, 7, 23949–23957.

32 M. C. Gélvez-Rueda, D. H. Cao, S. Patwardhan, N. Renaud, C. C. Stoumpos, G. C. Schatz, J. T. Hupp, O. K. Farha, T. J. Savenije, M. G. Kanatzidis and F. C. Grozema, J. Phys. Chem. C, 2016, 120, 16577–16585.

33 M. C. Gélvez-Rueda, E. M. Hutter, D. H. Cao, N. Renaud, C. C. Stoumpos, J. T. Hupp, T. J. Savenije, M. G. Kanatzidis and F. C. Grozema, J. Phys. Chem. C, 2017, 121, 26566–26574.

Supporting Information

Possibilities and limitations of $CsBi_3I_{10}$ as photovoltaic material

Paz Sebastia-Luna,[a] María C. Gélvez-Rueda,[b] Chris Dreessen,[a] Michele Sessolo,[a] Ferdinand C. Grozema,[b] Francisco Palazon,[a*] and Henk J. Bolink[a]

[a]Instituto de Ciencia Molecular, ICMol, Universidad de Valencia, St. Catedrático J. Beltrán 2, 46980 Paterna, Spain

[b]Department of Chemical Engineering, Opto-electronic Materials Section, Delft University of Technology, van der Maasweg 9, 2629 HZ Delft, The Netherlands

EXPERIMENTAL DETAILS

Materials

Caesium iodide (CsI, >99%) was obtained from TCI. Bismuth (III) iodide (BiI_3, ≥99.998%), fullerene (C_{60}) and chlorobenzene (99.8%, anhydrous) were purchased from Sigma Aldrich. Poly[N,N'-bis(4-butylphenyl)-N,N'-bis(phenyl)benzidine] (poly-TPD) was purchased from ADS Dyesource. N4,N4,N4′,N4′-tetra([1,1′-biphenyl]-4-yl)-[1,1′:4′,1′-terphenyl]-4,4′-diamine (TaTm) was provided by Novaled GmbH. Molybdenum (VI) oxide (MoO_3) and bathocuproine (BCP) were purchased from Lumtec. Tin (IV) oxide (SnO_2, 15% in H_2O colloidal dispersion) was provided by Alfa Aesar. All chemicals were stored in a nitrogen-filled glovebox and used without further purification. Photolithographically patterned ITO coated glass substrates were purchased from Naranjo Substrates.

Mechanochemical Synthesis

Stoichiometric amounts of CsI:BiI_3 powders were weighted to the desired stoichiometry and mixed in a nitrogen-filled glovebox. Then, the precursors powders introduced under nitrogen in 10 mL zirconia jars with two zirconia beads of 10 mm in diameter, both from Retsch. Ball milling was performed with an MM-400 straight ball mill from Retsch at a frequency of 30 Hz for 90 minutes.

XRD characterization

X-ray diffraction scans were measured with a powder diffractometer model D8 Avance A25 Bruker brand equipped with CuKα anode. Single measurements were acquired with a range of 2θ = 10° to 50° and a step size of 2θ = 0.025°, in Bragg-Brentano geometry in air.

Thermal characterization

Thermogravimetric analysis were performed with a TA Discovery TGA550 (TA Instruments) equipped with a continuous flow of nitrogen. Measurements were carried out with a ramp of 10 °C/min from room temperature to 600 °C.

CsI:BiI_3 thermal co-deposition

Deposition and characterization of the thin films were carried out inside a clean-room ISO 7 10000. Glass substrates underwent an extensive cleaning procedure using subsequent sonication in water with soap,

deionized water and 2-propanol baths. Then, they were dried with an N_2 flow and placed in a UV Ozone cleaner for 15 minutes.

$CsBi_3I_{10}$ thin films were prepared by dual source vacuum deposition by co-deposition of the two precursors CsI and BiI_3 onto the aforementioned substrates. To obtain a 210 nm-thick film of CsBi3I10, the deposition parameters were as follows:

	Rate (Å/s)	Temperature (ºC)	Set final thickness (nm)	Chamber pressure (mbar)
CsI	0.4	408	58	10^{-6}
BiI3	1.3	191	180	

The thermal evaporator was placed in air, outside a glovebox. This fact made the calibration of the deposition rate for both reagents difficult, due to their high hygroscopicity. For this reason, we believe the temperatures and pressure are more reliable parameters in order to obtain reproducible results than the deposition rates and set thicknesses.

Optical characterization

UV-visible absorption spectra of the films and powders were collected using an integrating sphere coupled to an Avantes Avaspec-2048L optical detector (Avantes BV). Photoluminescence for powders was measured with a continuous wave 522 nm laser diode with a 550 nm coloured glass filter (Thorlabs Inc.) and an Avantes Avaspec-2048L optical detector (Avantes BV), inside a nitrogen-filled glovebox. For a typical measurement, three scans with an integration time of 100 ms were collected and averaged. The photoluminescence characteristics for the thin-films were studied using a Microscopy Hyperspectral Imager IMA VIS from Photon Etc, coupled to a continuous-wave laser of 532 nm. For the analysis, the exposure time was set to 9 seconds and the field of view was 65x65 µm.

Scanning Electron Microscopy

SEM images were obtained using a Hitachi S-4800 Scanning-Electron Microscope, operating over platinum-metallized samples at an accelerating voltage of 20 kV.

Atomic Force Microscopy

Surface morphology of the co-evaporated thin-films was analysed using a Veeco Multimode SPM Atomic Force Microscopy (AFM).

Air Photoelectron Spectroscopy

The ionization energy of the materials was determined with an Ambient Pressure Photoemission Spectroscopy Systems (APS02) from KP Technology (KP Technology Ltd, Highlands and Islands, United Kingdom).

Device fabrication

Patterned ITO-covered glass substrates were cleaned using the same procedure as before. On top of them, a 5% aqueous solution of SnO_2 was deposited by spincoating and annealed at 150 ºC for 30 minutes to achieve a film thickness of 30 nm, approximately. After that, substrates were transferred into a vacuum chamber in a glovebox in order to deposit 10 nm of C_{60} at a pressure of 10^{-6} mbar. Subsequently, $CsBi_3I_{10}$ was deposited by co-evaporation of CsI and BiI_3 inside an air- placed vacuum thermal evaporator, following the same procedure as before. Then, a 15 nm-layer of TaTm and a 5 nm-layer of MoO_3 were consecutively deposited in a vacuum chamber inside a nitrogen-filled glovebox. To complete the devices, gold electrodes were evaporated until a thickness of 100 nm.

Device characterization

The electrical characterization was performed using a solar simulator by Abet Technologies (model 10500 with an AM1.5G xenon lamp as the light source). For calibrating the lamp, the exact light intensity was determined using a calibrated Si reference diode equipped with an infrared cut-off filter (KG-3, Schott). The layout used to test the solar cells has sixteen equal areas with an active area of 0.05 cm^2. J-V curves were recorded between -1 and 1.2 V with 0.01 V steps.

Pulsed-radiolysis time-resolved microwave conductivity (PR-TRMC)

PR-TRMC measurements determine the mobility and lifetime of charge carriers in crystalline semiconductor materials by irradiation with a high energy electron pulse (3 MeV) and probing with GHz microwaves. If after irradiation there are mobile charge carriers, they will absorb part of the microwave power. This decrease in microwave power is directly related to the changed of conductivity and ultimately to the mobility of charge carriers.[1] The crystalline powders (~45 mg) are placed in a Polyether ether ketone (PEEK) holder. The PEEK block with the sample is placed inside a rectangular waveguide cell (chemically inert gold-plated copper). The cell is contained in a cryostat in which the temperature can be varied between 123K and 473K. The irradiation intensity was varied between pulse lengths of 2 ns and 20 ns (charge carrier concentrations ~ $2x10^{16}$ cm^{--3} to $1x10^{17}$ $cm^{—3}$) at a frequency of 30.5 GHz. The frequency scan (28-38 GHz) fits were measured at a pulse length of 2 ns (~$2x10^{16}$ cm^{--3}).

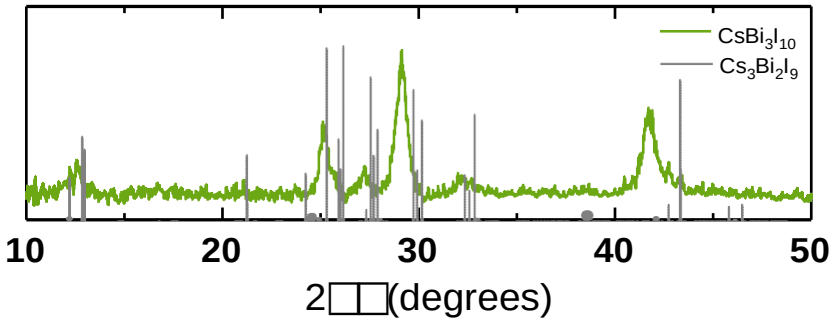

Figure S1. XRD diffractograms of the $CsBi_3I_{10}$ powders compared with the diffractograms for $Cs_3Bi_2I_9$, a specie that can be obtained with the same starting reagents as $CsBi_3I_{10}$.

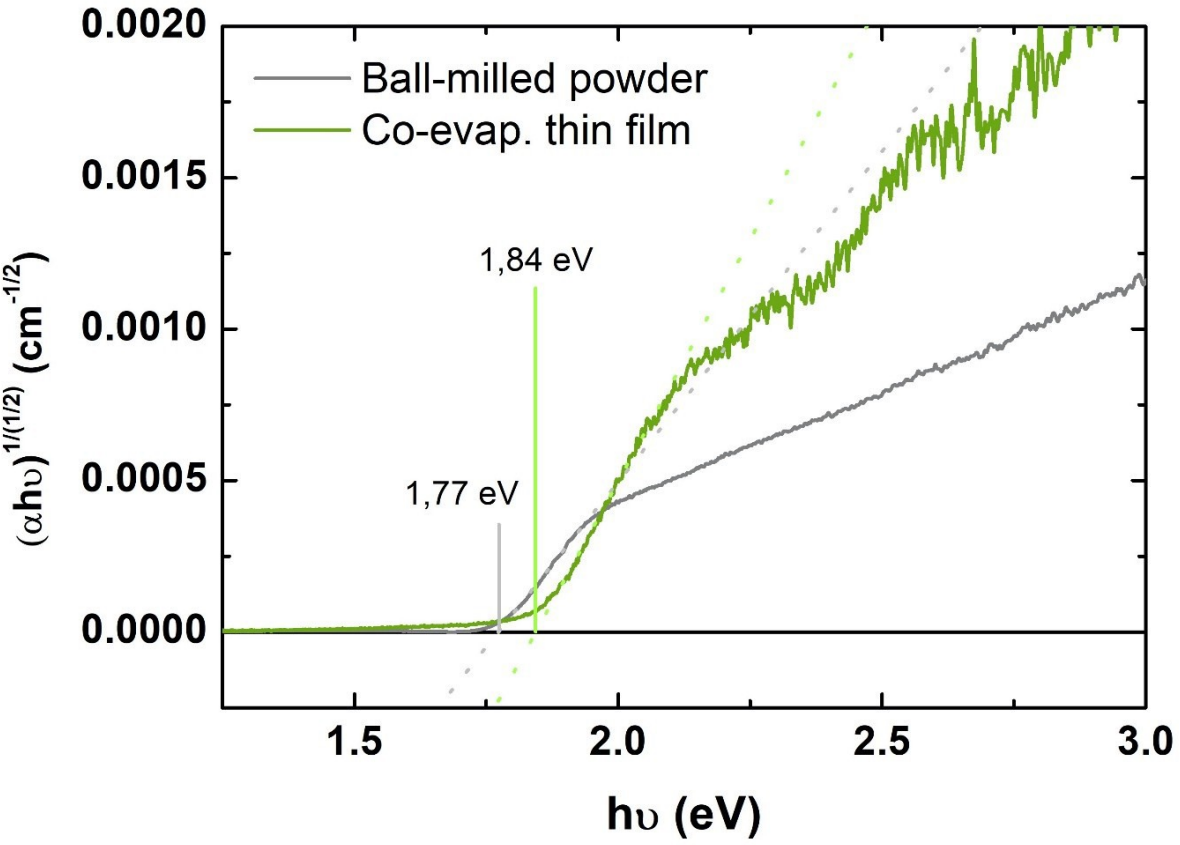

Figure S2. Tauc plots derived from optical absorbance of ball-milled and thin film samples. The slight mismatch in bandgap is discussed in the manuscript.

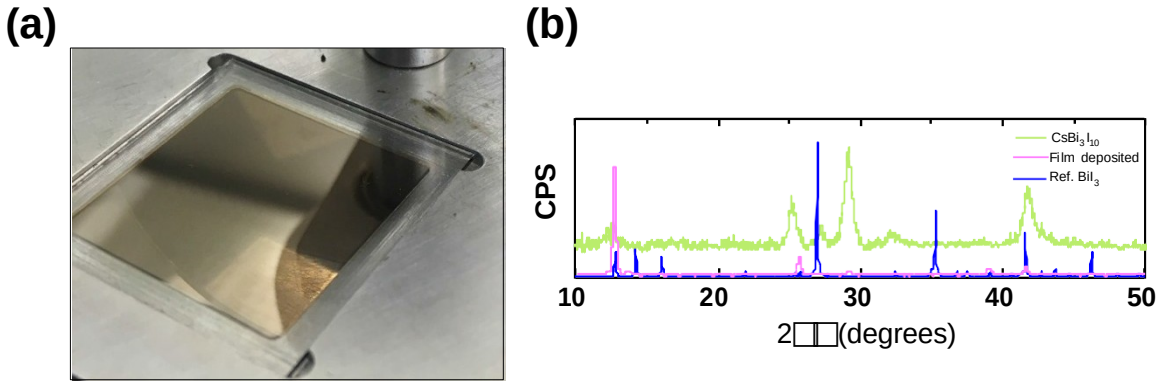

Figure S3. (a) Appearance of the thin film deposited by SSVD of $CsBi_3I_{10}$ and (b) XRD diffractograms of the $CsBi_3I_{10}$ in powder (starting material for the SSVD), the thin film obtained and BiI_3 (starting reagent of $CsBi_3I_{10}$). It is worth noting that the diffractogram of the thin film is different from the BiI3 in powder state, but not in thin film by thermal evaporation, as reported by other authors.[2,3]

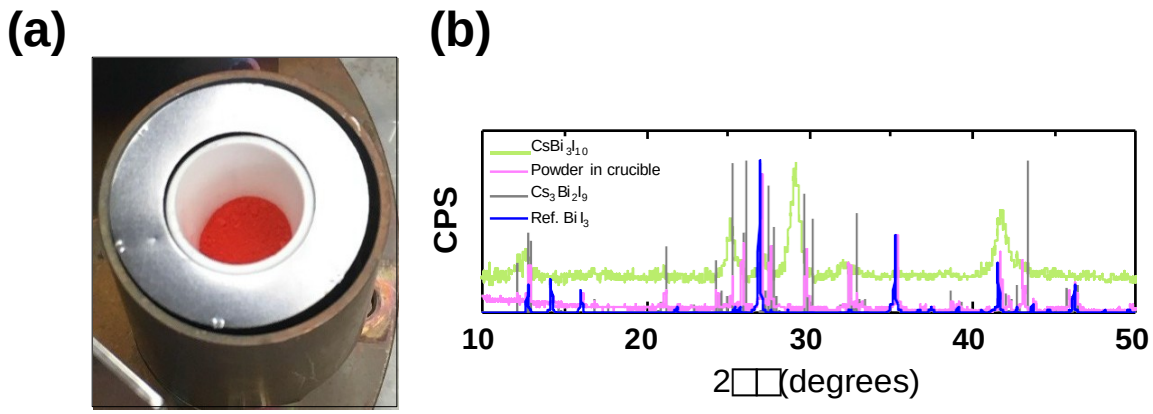

Figure S4. (a) Appearance of the remaining material in the crucible after the SSVD of $CsBi_3I_{10}$ and (b) XRD diffractograms of the $CsBi_3I_{10}$ in powder (starting material for the SSVD, green), the remaining powder in the crucible (pink), $Cs_3Bi_2I_9$ (possible decomposition product, grey) and BiI_3 (starting reagent of $CsBi_3I_{10}$, ICSD 56573, blue).

Table S1. Ratios of Cs:Bi:I for each temperature of annealing, calculated from XPS measurements. Calculations have been done taking the ideal stoichiometry (10) of iodide as a reference.

Temperature	Cs 3d	Bi 4f	I 3d
Pristine	1.55	2.81	10
50 °C	0.92	3.38	10
80 °C	1.04	3.37	10

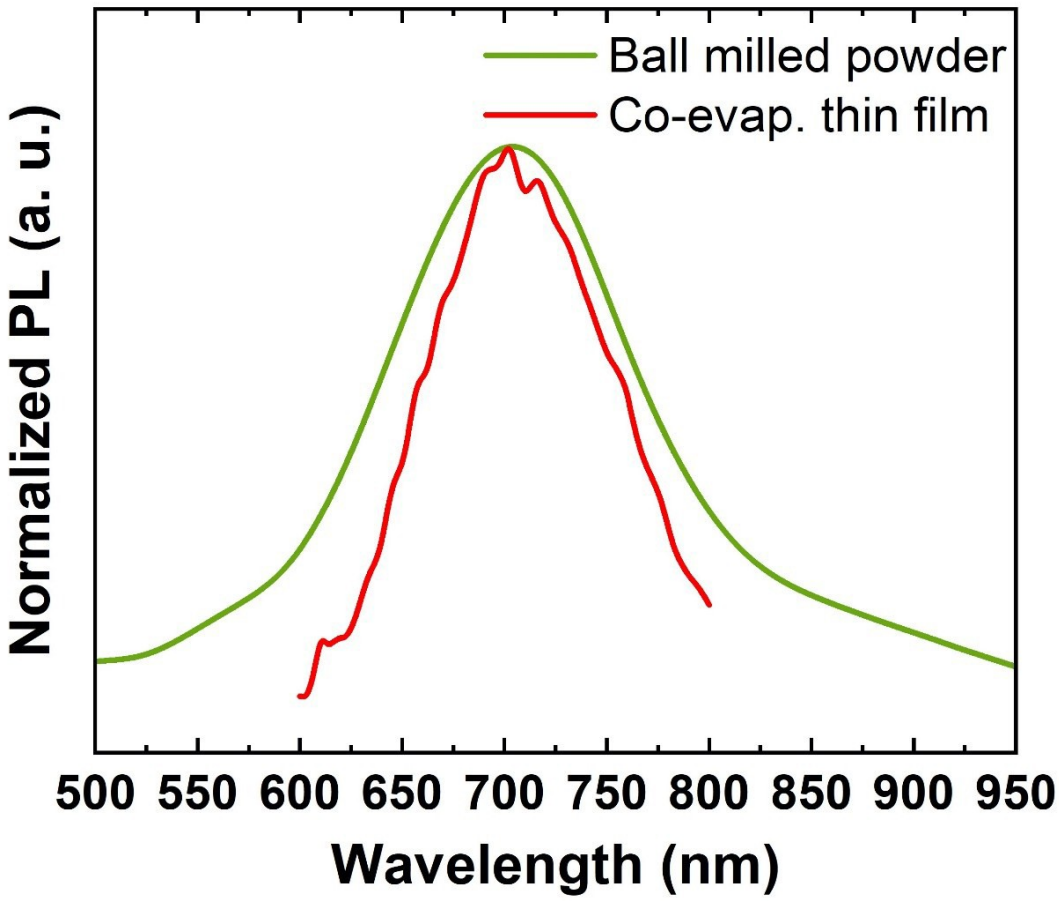

Figure S 5. Overlayed normalized PL spectra of thin film and powder sample. Differences in FWH are discussed in the main text.

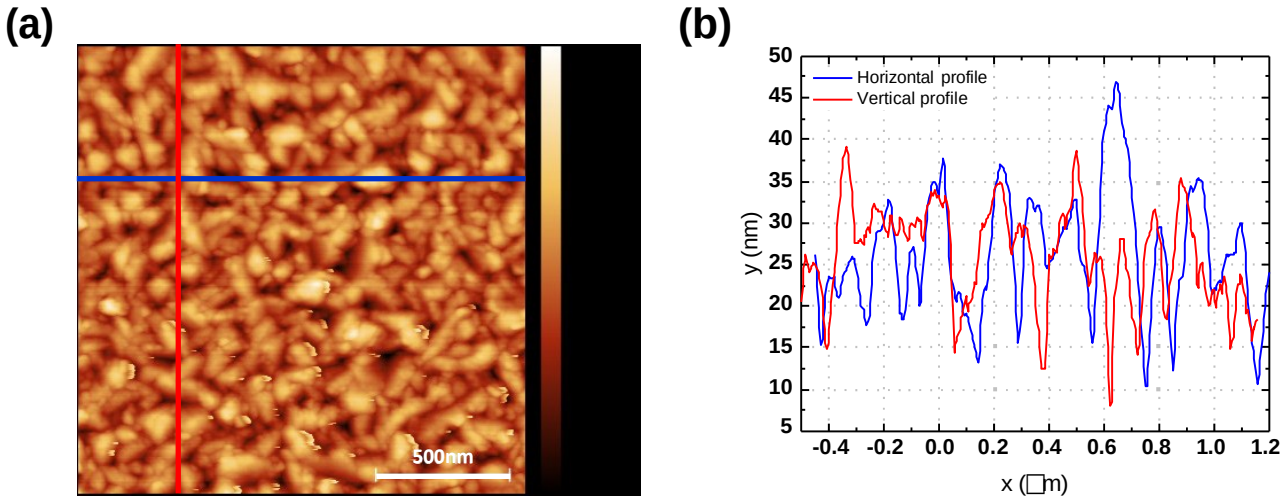

Figure S6. AFM topography (a) and horizontal and vertical profile indicating the roughness of the surface (b) of a $CsBi_3I_{10}$ thin-film deposited by co-evaporation.

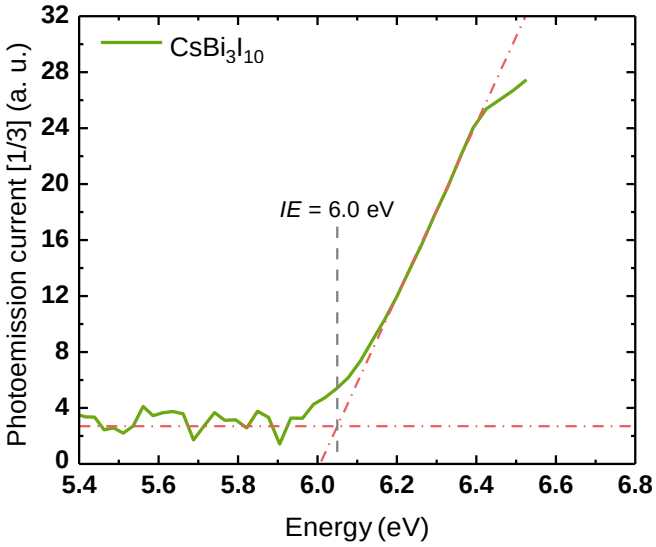

Figure S7. Photoemission spectra in air (APS) of $CsBi_3I_{10}$.

Table S2. Energy states for $CsBi_3I_{10}$. Values for energy levels are negative as they are referred to the VL.

Compound	***Bandgap (eV)***	***VBM (eV)***	***CBM (eV)***
$CsBi_3I_{10}$	1.8	-6.0	-4.2

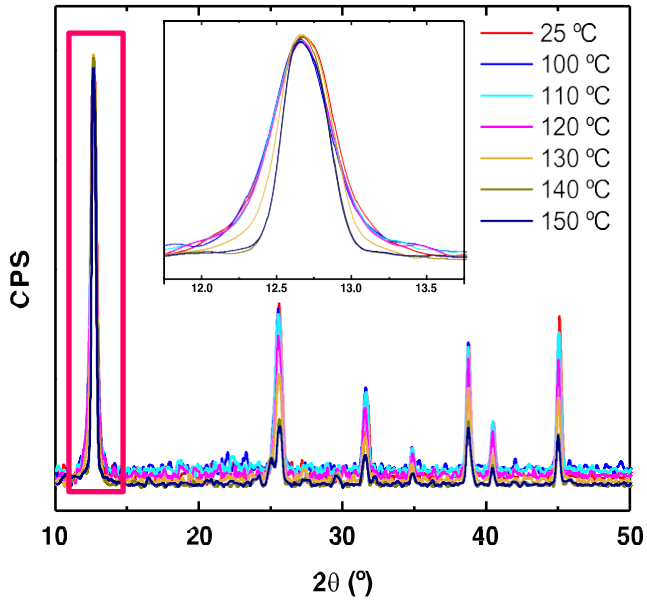

Figure S8. Overlay of X-Ray diffractograms at variable temperatures of a $CsBi_3I_{10}$ thin-film. A special inset is given for the specified region (in red) to show the sharpening of the peaks upon annealing. Applying Scherrer formula to the 25ºC and 150ºC samples, a grain growth from 24.3 nm to 27.9 nm is obtained. While the growth is undeniable, the absolute values are most likely underestimated as instrumental broadening is unknown and therefore not taken into account.

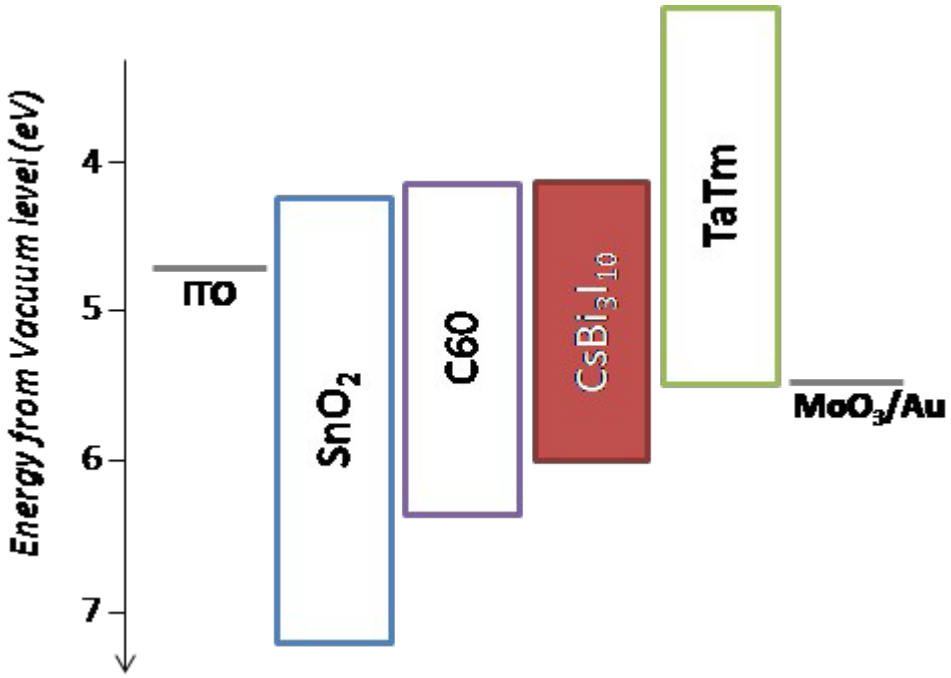

Figure S 9. Flat band energy diagram for the set of materials used in thin-film solar cells. Data for $CsBi_3I_{10}$ are estimated from APS measurements and the bandgap, the rest are from literature.

SUPPLEMENTARY REFERENCES:

1 J. Warman, M. De Haas, G. Dicker and F. Grozema, *Chem. Mater*, 2004, 4600–4609.

2 N. F. Coutinho, S. Cucatti, R. B. Merlo, J. M. C. Silva Filho, N. F. B. Villegas, F. Alvarez, A. F. Nogueira and F. C. Marques, *Sci. Rep.*, 2019, **9**, 11785.

3 N. F. Coutinho, R. B. Merlo, N. F. V. Borrero and F. C. Marques, *MRS Adv.*, 2018, **3**, 3233–3236.